

Article

# A Wideband Noise and Harmonic Distortion Canceling Low-Noise Amplifier for High-Frequency Ultrasound Transducers

Yuxuan Tang <sup>1</sup>, Yulang Feng <sup>1</sup>, He Hu <sup>2</sup>, Cheng Fang <sup>2</sup>, Hao Deng <sup>1</sup>, Runxi Zhang <sup>3</sup>, Jun Zou <sup>2</sup> and Jinghong Chen <sup>1,\*</sup>

- <sup>1</sup> Department of Electrical and Computer Engineering, University of Houston, Houston, TX 77004, USA; ytang11@uh.edu (Y.T.); yfeng19@uh.edu (Y.F.); hdeng3@uh.edu (H.D.)
- <sup>2</sup> Department of Electrical and Computer Engineering, Texas A&M University, College Station, TX 77843, USA; cn\_hu\_he@hotmail.com (H.H.); fangchengok2007@tamu.edu (C.F.); junzou@ece.tamu.edu (J.Z.)
- <sup>3</sup> School of Communication and Electronic Engineering, East China Normal University, Shanghai 200241, China; rxzhang@ee.ecnu.edu.cn
- \* Correspondence: jchen70@central.uh.edu; Tel.: +1-713-743-6096

**Abstract:** This paper presents a wideband low-noise amplifier (LNA) front-end with noise and distortion cancellation for high-frequency ultrasound transducers. The LNA employs a resistive shunt-feedback structure with a feedforward noise-canceling technique to accomplish both wideband impedance matching and low noise performance. A complementary CMOS topology was also developed to cancel out the second-order harmonic distortion and enhance the amplifier linearity. A high-frequency ultrasound (HFUS) and photoacoustic (PA) imaging front-end, including the proposed LNA and a variable gain amplifier (VGA), was designed and fabricated in a 180 nm CMOS process. At 80 MHz, the front-end achieves an input-referred noise density of 1.36 nV/sqrt (Hz), an input return loss ( $S_{11}$ ) of better than  $-16$  dB, a voltage gain of 37 dB, and a total harmonic distortion (THD) of  $-55$  dBc while dissipating a power of 37 mW, leading to a noise efficiency factor (NEF) of 2.66.

**Keywords:** high-frequency ultrasound transducers; low-noise amplifier; noise cancellation; harmonic distortion cancellation; resistive shunt-feedback amplifier; wideband impedance matching



**Citation:** Tang, Y.; Feng, Y.; Hu, H.; Fang, C.; Deng, H.; Zhang, R.; Zou, J.; Chen, J. A Wideband Noise and Harmonic Distortion Canceling Low-Noise Amplifier for High-Frequency Ultrasound Transducers. *Sensors* **2021**, *21*, 8476. <https://doi.org/10.3390/s21248476>

Academic Editor: Andrea Cataldo

Received: 16 November 2021

Accepted: 17 December 2021

Published: 19 December 2021

**Publisher's Note:** MDPI stays neutral with regard to jurisdictional claims in published maps and institutional affiliations.



**Copyright:** © 2021 by the authors. Licensee MDPI, Basel, Switzerland. This article is an open access article distributed under the terms and conditions of the Creative Commons Attribution (CC BY) license (<https://creativecommons.org/licenses/by/4.0/>).

## 1. Introduction

With the recent advancements of high-frequency ( $>30$  MHz) ultrasound transducers [1], such as polyvinylidene fluoride (PVDF) piezoelectric transducers and capacitive micromachined transducers (CMUT), high-frequency ultrasound and photoacoustic imaging have been developed rapidly. The HFUS and PA imaging with improved microscopic resolutions opens many new medical imaging applications [2–7] in the fields of ophthalmology, dermatology, photoacoustic microscope, intravascular imaging (IVUS), and systemic sclerosis (SSC).

In HFUS and PA imaging, ultrasound transducers are utilized to detect the acoustic pressure transients and to generate electrical signals accordingly. The electrical signals are then processed by the ultrasonic imaging receiver, in which the low-noise amplifier (LNA) is the key component. To support HFUS and PA imaging, the LNA needs to achieve low noise and high bandwidth simultaneously. Conventionally, the LNA is designed as either a charge-sensitive amplifier (CSA) or a voltage amplifier. Although the CSA provides low noise performance [8,9], the feedback loop formed by the bleeding resistor and the feedback capacitor significantly limits the achievable amplifier bandwidth. The voltage-mode amplifier, such as the resistive shunt-feedback amplifier in [10], achieves large bandwidth and wideband impedance matching, however, the noise performance is poor due to the fixed transconductance of the input transistor for the impedance matching. To improve the

noise performance of voltage-mode amplifiers, noise-canceling (NC) techniques [11–13] have been recently explored. Reference [12] proposes an LNA utilizing a combination of a common-gate (CG) amplifier and a common-source (CS) amplifier for noise cancellation. Nonetheless, the pseudo-differential structure is prone to gain a mismatch between the CG and CS gain stages. Based on a resistive shunt-feedback amplifier structure, our recent work [13] also demonstrates a noise-canceling wideband LNA, where a common-source auxiliary amplifier is employed to generate an in-phase signal and an out-of-phase noise, with respect to those of the main amplifier, for noise cancellation.

As the outputs of ultrasound transducers are normally in single-ended mode, the LNAs are typically limited to single-ended structures, thus suffering from even-order nonlinear distortion. To suppress the even-order harmonics, single-ended-to-differential conversion circuits have been utilized but with the penalties of additional noise and power consumption. To address this issue, a bulky LC resonator is used as a band-pass filter in [14] to reject the second-order harmonic distortion. In [15], a constant transconductance structure is developed to achieve second-order intermodulation distortion (IM<sub>2</sub>) cancellation. The constant transconductance, however, relies on precisely matched triode transistors.

Power consumption is also a major concern in designing ultrasound LNAs. In beam-forming applications where multiple channels are integrated on a single chip, the heat generated by the LNAs can significantly affect chip reliability. Low power consumption is also indispensable in portable ultrasound systems. To reduce LNA power consumption, a step-up balun with two secondary turns is developed in [16] to alleviate the transconductance requirement for impedance matching. The use of balun, however, is not applicable to wideband ultrasound LNAs because of its large area penalty.

In this article, which is an extension of [13,17], a complementary resistive shunt-feedback LNA with both noise and distortion cancellations is presented to simultaneously achieve wideband impedance matching, low noise, and high linearity for HFUS and PA imaging applications. An electrical model of the PVDF ultrasound transducer is also developed to guide the LNA design process. Designed in a 180 nm CMOS technology, the LNA achieves a 0.8 nV/sqrt (Hz) input-referred voltage noise density, a 19 dB voltage gain, and a −59.3 dBc total harmonic distortion (THD) at 80 MHz. An ultrasound front-end with the proposed LNA and a pseudo-differential variable gain amplifier (VGA) is also designed and fabricated. At 80 MHz, measurements show that the front-end achieves an input-referred voltage noise density of 1.36 nV/sqrt (Hz), a better than −16 dB input return loss (S<sub>11</sub>), a voltage gain of 37 dB, and a THD of −55 dBc. The front-end consumes 37 mW of power from a 1.8 V supply and achieves a noise efficiency factor (NEF) of 2.66.

The overall LNA design was carried out by the following procedures. First, the typical electrical parameters of the PVDF ultrasound transducer for HFUS and PA imaging applications were obtained through experimental measurements. The parameters included the resonance frequency, output impedance, and output amplitude of the transducer. Then, an electrical model of the PVDF transducer was developed to facilitate the co-simulation of the LNA with the ultrasound transducer. Second, given the typical PVDF electrical parameters, the LNA design specifications, including gain and bandwidth, input impedance matching, and total harmonic distortion, were defined. Design solutions for improving the bandwidth, noise, linearity, and power efficiency of the LNA were then developed. A test chip was designed and fabricated in a 180 nm CMOS technology, and experimental measurements were carried out to validate the proposed LNA design solutions.

The remainder of this paper is organized as follows. Section 2 describes the model development of the PVDF transducer. Section 3 presents the LNA design solutions for improving bandwidth, noise, linearity, and power efficiency. Section 4 describes the proposed LNA design in a 180 nm CMOS technology. Section 5 presents the chip measurement results and Section 6 concludes the paper.

## 2. PVDF Ultrasound Transducer Model

Figure 1a depicts the schematic of the ultrasound transducer, which was made of a 9- $\mu\text{m}$ -thick piezoelectric material PVDF film, whose resonance frequency and bandwidth were around 50~80 MHz and 75~140 MHz, respectively [18–20]. The materials of the transducer electrodes were Indium Tin Oxide (ITO) and Aluminum (Al). The fabrication process was conducted as follows: (1) A 9- $\mu\text{m}$ -thick polarized PVDF film was cut into pieces of suitable sizes; (2) With RF sputtering, the 200-nm-thick ITO electrodes were formed on the two surfaces of the PVDF film; (3) With DC sputtering, the aluminum electrodes were formed on the surfaces of the PVDF film. The effective sensing region was the  $2 \times 2 \text{ mm}^2$  transparent area at the center. Figure 1b shows the photograph of the PVDF transducer and its electrical model. Measured with an impedance analyzer, Figure 2 presents the electrical output impedance of the transducer, where the series resistance  $R_s$  was about  $50 \Omega$  from 50 MHz to 100 MHz and the series capacitance  $C_s$  was close to a constant of 16 pF.

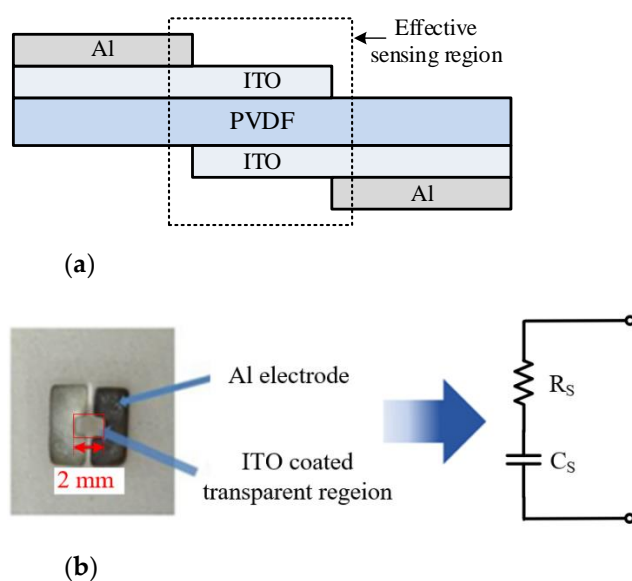


**Figure 1.** (a) Schematic diagram of the PVDF transducer; (b) photograph of the PVDF transducer and its electrical model.

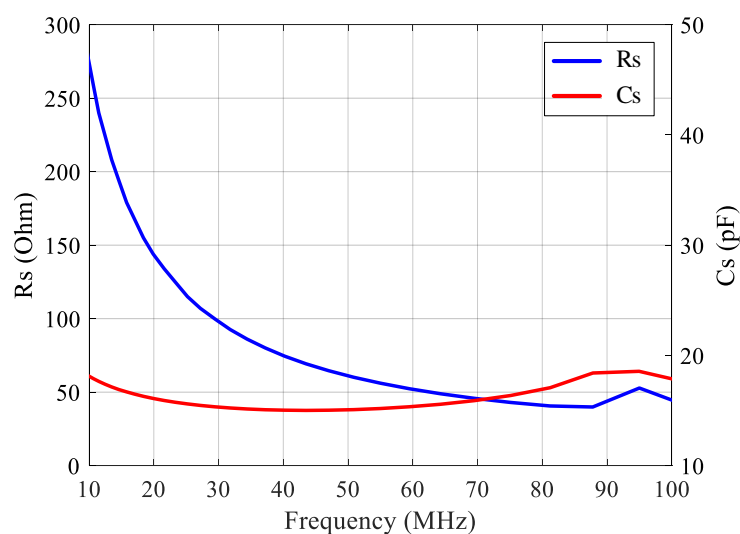
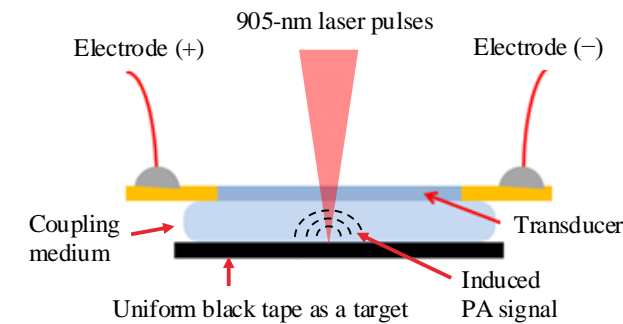


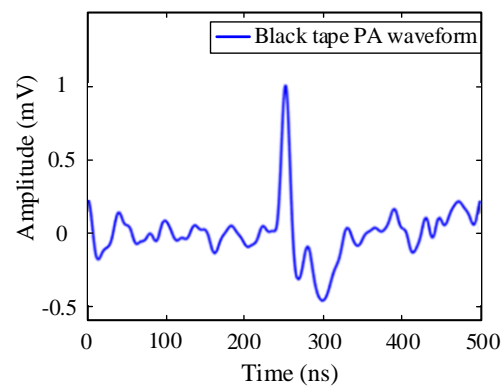
**Figure 2.** Measured output impedance of the PVDF transducer.

As shown in Figure 3a, to measure the photoacoustic response of the transducer, an optically absorptive target made of black tape was used. The target was put under the

transducer's effective sensing region. During the measurement, a small amount of water was added between the transducer and the target surface to improve the acoustic signal coupling efficiency. The 905-nm laser pulses (pulse width: 8 ns, pulse energy: 150 nJ/pulse, repetition rate: 1 kHz) were shot through the transducer to the target. The PA signal excited from the surface of the target was detected by the transducer. The representative PA signal recorded by the transducer is depicted in Figure 3b.



(a)



(b)

**Figure 3.** (a) Measurement setup for the PA response of the PVDF transducer; (b) recorded PA signal induced by laser pulse onto black tape.

Given that the typical resonance frequency of the PVDF transducer was about 50–80 MHz where the corresponding  $R_s$ , as shown in Figure 2, was about  $50 \pm 10 \Omega$  and that the typical transducer output signal was 1 mV, as shown in Figure 3b, the LNA along with the post amplifier was thus designed to aim to achieve about 40 dB voltage gain,  $-50$  dBc THD under 1 mV input, and a better than  $-15$  dB input return loss across the transducer resonance frequency range.

### 3. LNA Design and Analysis

#### 3.1. Resistive Shunt-Feedback

The resistive shunt-feedback amplifier, as depicted in Figure 4, was chosen as the basic building block for the proposed high-frequency LNA. The resistive shunt-feedback structure simultaneously offered a high  $f_{-3dB}$  bandwidth and wideband impedance matching.

Neglecting the effect of parasitic capacitance  $C_{gs}$  of the input transistor  $M_1$  and assuming  $R_L \gg R_F$ , the input impedance of the shunt-feedback amplifier could be derived as

$$Z_{IN} = \frac{R_F + R_L}{1 + g_{m1}R_L} \approx \frac{1}{g_{m1}}, \quad (1)$$

where  $g_{m1}$  is the transconductance of transistor  $M_1$ . The input impedance matching condition was then obtained as

$$R_S = Z_{IN} = \frac{1}{g_{m1}}, \quad (2)$$

where  $R_S$  is the source impedance.

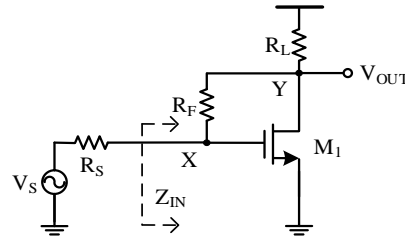


**Figure 4.** Resistive shunt-feedback amplifier with high bandwidth and wideband impedance matching [13].

Next, we derived the signal gain of the amplifier  $\frac{V_{Y,S}}{V_S}$ . The gain from node X to node Y was derived as

$$\frac{V_{Y,S}}{V_{X,S}} = \frac{(1 - g_{m1}R_F)R_L}{R_F + R_L} \approx 1 - g_{m1}R_F, \quad (3)$$

where  $V_{Y,S}$  and  $V_{X,S}$  are the signals at the amplifier output node and the gate node of transistor  $M_1$ , respectively. Then, under the input impedance matched condition, the signal gain  $\frac{V_{Y,S}}{V_S}$  was derived as

$$\frac{V_{Y,S}}{V_S} = \frac{V_{Y,S}}{V_{X,S}} \times \frac{V_{X,S}}{V_S} = (1 - g_{m1}R_F) \frac{R_S}{R_S + Z_{IN}} = \frac{1}{2} \left( 1 - \frac{R_F}{R_S} \right). \quad (4)$$

The major noise components of the amplifier were the thermal noises of  $R_S$  and the amplifier input transistor  $M_1$ . The noise factor of the amplifier [11] could be derived as

$$F > 1 + \frac{4kT\gamma \times Z_{IN}}{4kTR_S} + \chi = 1 + \gamma + \chi > 2, \quad (5)$$

where  $k$  is the Boltzmann's constant,  $T$  is the temperature in Kelvins,  $\gamma$  is the channel thermal noise coefficient and  $1 < \gamma < 2$  for submicron n-channel MOSFETs [21], and  $\chi$  represents the flicker noise and the thermal noise induced by other parts of the circuit (e.g.,  $R_F$  and  $R_L$ ). From Equation (5), the achievable noise figure (NF) was larger than 3 dB and was often larger than 5 dB practically. The noise performance of the wideband resistive shunt-feedback amplifier clearly needs to be improved.

### 3.2. Feedforward Noise Cancellation

To improve the noise performance, feedforward noise cancellation [13] was exploited. Figure 5 depicts the noise-canceling technique where an auxiliary amplifier was used to generate an in-phase signal and an out-of-phase noise with respect to those of the main amplifier  $M_1$ . The main amplifier  $M_1$  had an inverting signal gain, as shown in Equation (4). The noise gain of the main amplifier  $M_1$  could be derived as

$$\frac{V_{Y,N}}{V_{X,N}} = 1 + \frac{R_F}{R_S}, \quad (6)$$

where  $V_{X,N}$  denotes the input-referred thermal noise of  $M_1$ , and  $V_{Y,N}$  is the corresponding output noise. From Equation (6), the main amplifier  $M_1$  had a non-inverting gain for noise. To cancel the noise of  $M_1$ , the auxiliary amplifier, as shown in Figure 5, was designed to have an inverting amplification for both the signal and the noise at node X. With the main

amplifier and the auxiliary amplifier exhibiting opposite noise gains, noise cancellation can thus be achieved.

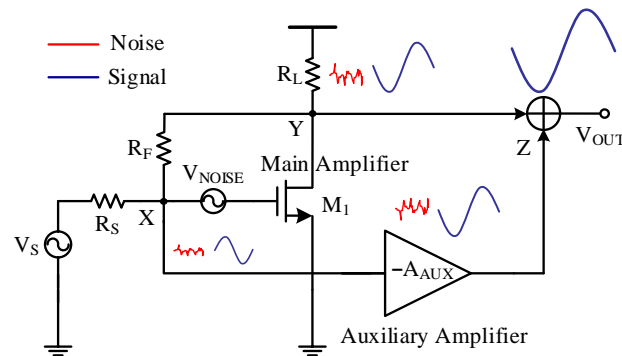


**Figure 5.** Block diagram of the feedforward noise-canceling technique [13].

Figure 6 shows the transistor-level implementation of the noise-canceling resistive shunt-feedback LNA, where transistor  $M_1$  worked as the main amplifier,  $M_2$  with a cascode structure worked as the auxiliary amplifier, and  $M_4$  worked as a source follower combining the outputs of both amplifiers. The main amplifier and the auxiliary amplifier were connected in parallel with respect to node X. The input impedance condition of the LNA could be derived to be the same as in Equation (2).

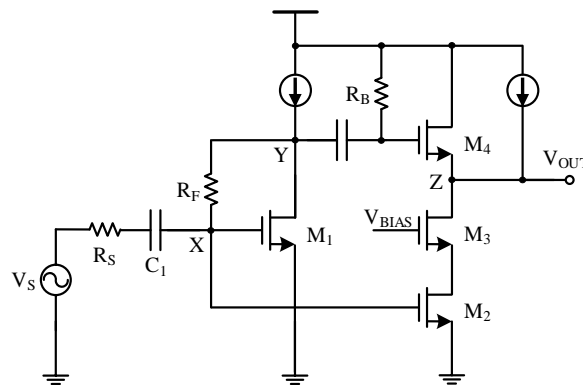


**Figure 6.** Noise-canceling resistive shunt-feedback LNA [13].

Ignoring the small gain reduction due to the source follower, the signal gain  $\frac{V_{Z,S,M}}{V_S}$  and the noise gain  $\frac{V_{Z,N,M}}{V_{X,N}}$  at node Z contributed by the main amplifier could be obtained as

$$\frac{V_{Z,S,M}}{V_S} = \frac{V_{Y,S,M}}{V_S} = \frac{1}{2} \left( 1 - \frac{R_F}{R_S} \right), \quad (7)$$

and

$$\frac{V_{Z,N,M}}{V_{X,N}} = \frac{V_{Y,N,M}}{V_{X,N}} = 1 + \frac{R_F}{R_S}. \quad (8)$$

The signal gain  $\frac{V_{Z,S,A}}{V_S}$  and the noise gain  $\frac{V_{Z,N,A}}{V_{X,N}}$  of the auxiliary amplifier were derived as

$$\frac{V_{Z,S,A}}{V_S} = \frac{V_{Z,S,A}}{V_{X,S,A}} \times \frac{V_{X,S,A}}{V_S} = -\frac{1}{2} \frac{g_{m2}}{g_{m4}}, \quad (9)$$

and

$$\frac{V_{Z,N,A}}{V_{X,N}} = -\frac{g_{m2}}{g_{m4}}, \quad (10)$$

where  $g_{m2}$  and  $g_{m4}$  are the transconductance of transistors  $M_2$  and  $M_4$ , respectively.

With Equations (7)–(10), the noise-canceling condition at node Z could be obtained as

$$\begin{aligned} \frac{V_{Z,N,M}}{V_{X,N}} + \frac{V_{Z,N,A}}{V_{X,N}} &= \left(1 + \frac{R_F}{R_S}\right) - \frac{g_{m2}}{g_{m4}} = 0, \\ \implies 1 + \frac{R_F}{R_S} &= \frac{g_{m2}}{g_{m4}}, \end{aligned} \quad (11)$$

and the total signal gain  $A_{S,TOT}$  was given by

$$A_{S,TOT} = \frac{V_{Z,S,M}}{V_S} + \frac{V_{Z,S,A}}{V_S} = -\frac{R_F}{R_S}. \quad (12)$$

Under the noise-canceling condition in Equation (11), the noise of the main amplifier  $M_1$  was canceled by the auxiliary amplifier  $M_2$ . The input-referred noise of the overall amplifier was only determined by the auxiliary amplifier  $M_2$  and could be made small with a large  $g_{m2}$  without impairing the impedance matching condition, which is only determined by  $g_{m1}$  as shown in Equation (2). The LNA thus achieved both wideband impedance matching and low noise performance.

### 3.3. Complementary CMOS Topology

To suppress the second-order harmonics in the single-ended ultrasound LNA structure, complementary CMOS topology was investigated [17]. As depicted in Figure 7, the complementary CMOS amplifier consisted of a PMOS-based resistive shunt-feedback amplifier  $M_P$  in parallel with an NMOS-based resistive shunt-feedback amplifier  $M_N$ . The drain current in each sub-amplifier as a function of the input signal was respectively obtained as [22]:

$$i_{ds,P} = I_{DS,P} + g_{m,P}(-v_{gs}) + \frac{1}{2!}g'_{m,P}(-v_{gs})^2 + \frac{1}{3!}g''_{m,P}(-v_{gs})^3 + \dots, \quad (13)$$

and

$$i_{ds,N} = I_{DS,N} + g_{m,N}(v_{gs}) + \frac{1}{2!}g'_{m,N}(v_{gs})^2 + \frac{1}{3!}g''_{m,N}(v_{gs})^3 + \dots, \quad (14)$$

where  $g'_{m,P}$ ,  $g'_{m,N}$ ,  $g''_{m,P}$  and  $g''_{m,N}$  are the first-order and the second-order derivatives of the transconductances  $g_{m,P}$  and  $g_{m,N}$  with respect to the gate-to-source voltage  $v_{gs}$ , respectively.

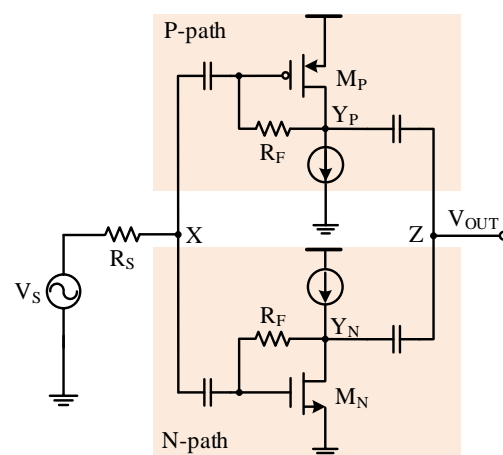


Figure 7. Complementary resistive shunt-feedback amplifier.

By summing the two currents, the output current of the complementary amplifier was obtained as

$$\begin{aligned} i_{out} &= i_{ds,N} - i_{ds,P} \\ &= (g_{m,N} + g_{m,P})(v_{gs}) + \frac{1}{2!}(g'_{m,N} - g'_{m,P})(v_{gs})^2 + \frac{1}{3!}(g''_{m,N} + g''_{m,P})(v_{gs})^3 + \dots \end{aligned} \quad (15)$$



From Equation (15), it can be observed that the second-order harmonic can be largely canceled if  $g'_{m,P} \approx g'_{m,N}$ . The simulated drain currents ( $i_{ds}$ ), the transconductance ( $g_m$ ), and the first-order derivative of the transconductance ( $g'_m$ ) of a 240- $\mu\text{m}/0.18\text{-}\mu\text{m}$  PMOS  $M_P$  and a 120- $\mu\text{m}/0.18\text{-}\mu\text{m}$  NMOS  $M_N$  are plotted in Figure 8. With proper biasing, the  $g_{m,P}$  and  $g_{m,N}$  can be well-defined to achieve  $g'_{m,P} \approx g'_{m,N}$ . As the second-order harmonic dominated the nonlinearity of the single-ended LNA, the proposed complementary CMOS amplifier structure provides a low-cost solution to attain good linearity while avoiding the noise and power consumption penalties of a dedicated single-ended-to-differential conversion circuit.

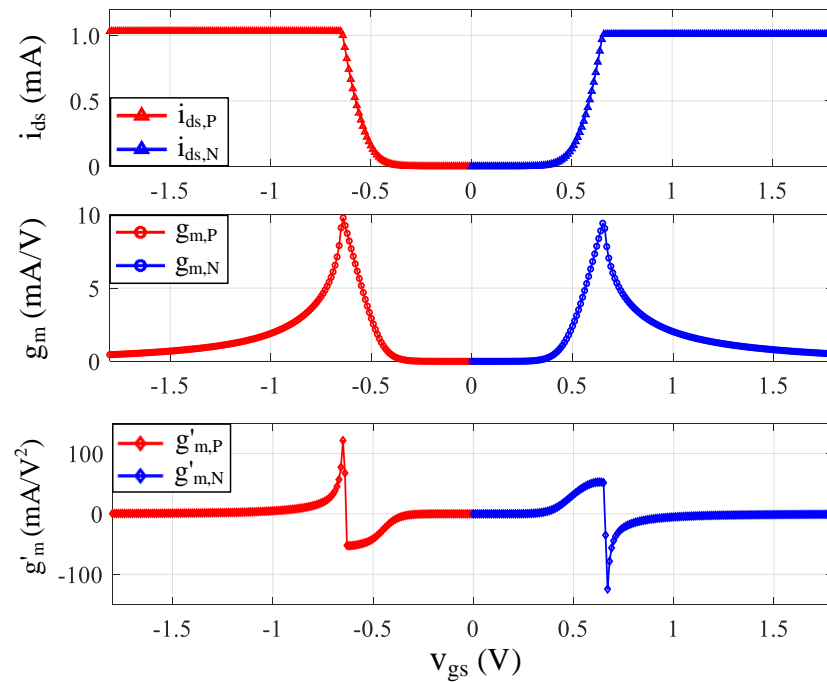


**Figure 8.** Simulated  $i_{ds}$ ,  $g_m$  and  $g'_m$  of a 240- $\mu\text{m}/0.18\text{-}\mu\text{m}$  PMOS  $M_P$  and a 120- $\mu\text{m}/0.18\text{-}\mu\text{m}$  NMOS  $M_N$  for the complementary resistive shunt-feedback amplifier.

With the complementary CMOS topology, the input impedance matching condition was jointly determined by both the  $M_P$  and  $M_N$  transistors and could be obtained as

$$R_S = Z_{IN} = \frac{1}{g_{m,P} + g_{m,N}}. \quad (16)$$

The signal gain of the complementary resistive shunt-feedback amplifier was derived as

$$\begin{aligned} \frac{V_{Z,S}}{V_S} &= \left( \frac{V_{Y,P,S}}{V_{X,S}} + \frac{V_{Y,N,S}}{V_{X,S}} \right) \times \frac{V_{X,S}}{V_S} = [(1 - g_{m,P}R_F) + (1 - g_{m,N}R_F)] \frac{R_S}{R_S + Z_{IN}} \\ &= \frac{1}{2} \left( 2 - \frac{R_F}{R_S} \right). \end{aligned} \quad (17)$$

### 3.4. Current-Reuse Technique

To reduce the power consumption of the LNA, the current-reuse technique [23] was investigated. Modifying the complementary amplifier in Figure 7 by stacking the P-path amplifier with the N-path amplifier and removing the biasing current sources, the current-reuse resistive shunt-feedback amplifier was constructed and is shown in Figure 9.



The input impedance matching condition of the current-reuse amplifier was similar to Equation (16) and was obtained as

$$R_S = Z_{IN} = \frac{R_F + r_{out,P,CR} // r_{out,N,CR}}{1 + (g_{m,P,CR} + g_{m,N,CR}) \times r_{out,P,CR} // r_{out,N,CR}} \approx \frac{1}{g_{m,P,CR} + g_{m,N,CR}}, \quad (18)$$

where  $g_{m,P,CR}$  and  $g_{m,N,CR}$  are the transconductance of transistors  $M_{P,CR}$  and  $M_{N,CR}$ , respectively, assuming  $r_{out,P,CR} // r_{out,N,CR} \gg R_F$ . Under the input impedance matched condition, the signal gain was derived with the superposition principle as

$$\frac{V_{Z,S}}{V_S} = \frac{V_{Z,S}}{V_{X,S}} \times \frac{V_{X,S}}{V_S} = \frac{1}{2} [(1 - g_{m,P,CR} R_F) + (1 - g_{m,N,CR} R_F)] = \frac{1}{2} \left( 2 - \frac{R_F}{R_S} \right), \quad (19)$$

which was the same as Equation (17). In the current-reuse structure, the  $M_{P,CR}$  and  $M_{N,CR}$  needed to be sized so that the output common-mode voltage was close to half  $V_{DD}$ . The input common-mode voltage was set by the output common-mode voltage through the feedback resistor  $R_F$ . Compared to the complementary resistive shunt-feedback amplifier in Figure 7, the current-reuse structure only required half of the DC current to maintain the impedance matching condition, thus reducing the amplifier power consumption by almost half. Removing the biasing current sources also allowed a low supply voltage to be used, as long as  $M_{P,CR}$  and  $M_{N,CR}$  were in saturation, which helped to further reduce the power consumption.

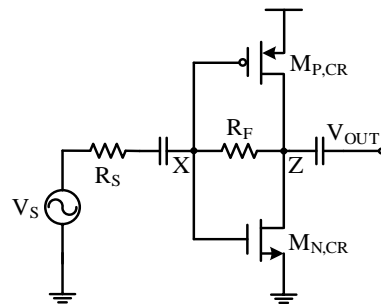


Figure 9. Current-reuse resistive shunt-feedback amplifier.

Simulation results [24] showed that the path stacking of the complementary resistive shunt-feedback amplifier brought a 1.2 mA DC current reduction and the use of a 1.3 V supply further reduced the power consumption by 9 mW, while the LNA could still maintain a  $f_{-3dB}$  bandwidth of larger than 150 MHz. The use of a low  $V_{DD}$ , however, mandated large sized transistors, especially in the auxiliary amplifiers, to maintain low noise performance. This led to a large parasitic capacitance at the amplifier input node, which could degrade the amplifier  $S_{11}$  at high frequencies. In designing the low- $V_{DD}$  current-reuse amplifier with feedforward noise-canceling, the  $V_{DD}$  needs to be properly selected to tradeoff between noise, power saving, bandwidth, and high-frequency  $S_{11}$ .

#### 4. Proposed LNA Design

A resistive shunt-feedback LNA with the feedforward noise-canceling technique and the complementary topology was designed in a 180 nm CMOS technology. As shown in Figure 10, the complementary topology was formed of both the N-path and the P-path amplifiers, where each path employed resistive shunt-feedback with feedforward noise cancellation. In the figure,  $M_{1P}$  and  $M_{1N}$  are the main amplifiers,  $M_{2P}$  and  $M_{2N}$  are the auxiliary amplifiers, and  $M_{4P}$  and  $M_{4N}$  are the analog combiners, respectively. The sizes of the  $M_{1P}$  and  $M_{1N}$  transistors were  $240\text{-}\mu\text{m}/0.18\text{-}\mu\text{m}$  and  $120\text{-}\mu\text{m}/0.18\text{-}\mu\text{m}$ , respectively. Both transistors were biased with 1 mA current. The corresponding  $g_{m,1P}$  and  $g_{m,1N}$  were 9.81 mA/V and 9.57 mA/V, respectively, leading to an input impedance  $Z_{IN}$  of about

51.6  $\Omega$ . The corresponding  $g'_{m,1P}$  was 67 mA/V<sup>2</sup> and  $g'_{m,1N}$  was 61 mA/V<sup>2</sup> and this helped to achieve the cancellation of the second-order harmonic distortion. The size of the  $M_{2P}$  and  $M_{2N}$  transistors were designed as 960- $\mu\text{m}/0.18\text{-}\mu\text{m}$  and 480- $\mu\text{m}/0.18\text{-}\mu\text{m}$  with the corresponding  $g_{m,2P}$  being 36.3 mA/V and  $g_{m,2N}$  being 38.3 mA/V to achieve low noise performance.

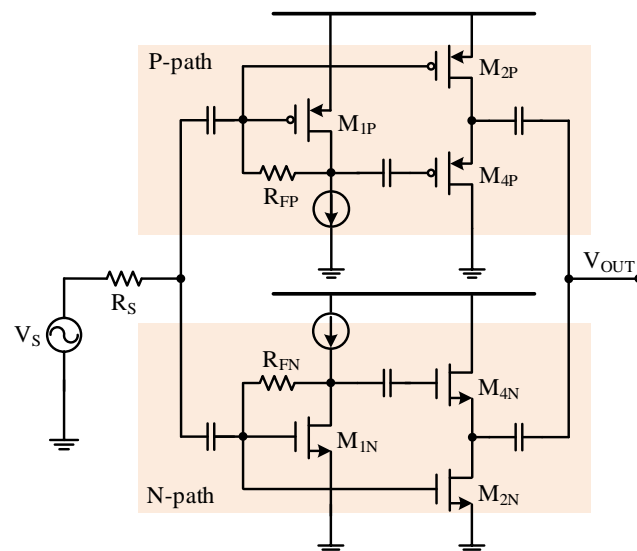


**Figure 10.** Proposed resistive shunt-feedback LNA with the feedforward noise-canceling technique and the complementary topology [17].

Figures 11 and 12 show the simulated  $S_{11}$  and frequency response of the LNA, respectively. The  $S_{11}$  was better than  $-17$  dB over the desired ultrasound transducer operation frequency range. The  $S_{11}$  at higher frequencies was slightly degraded by the main amplifier input node capacitance. The frequency response shows that the LNA had a gain of 19 dB, up to 120 MHz, in the typical corner and a  $f_{-3\text{dB}}$  bandwidth of 770 MHz. The gain variation over the process, voltage, and temperatures (PVTs) was less than 2 dB.

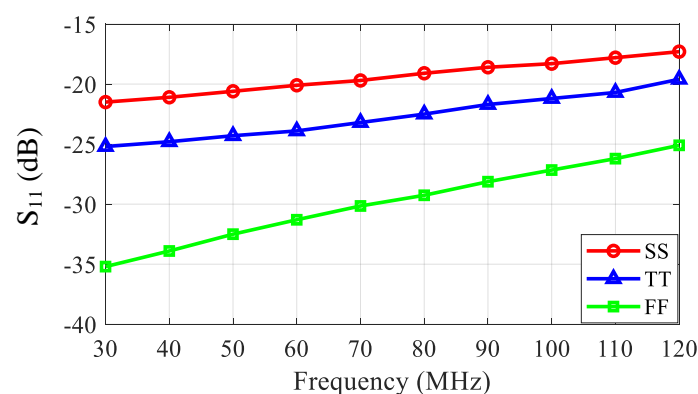


**Figure 11.** Simulated  $S_{11}$  of the proposed LNA, where SS, TT, and FF stand for the slow PMOS and NMOS, typical PMOS and NMOS, and fast PMOS and NMOS process corners, respectively.

As shown in Figure 13, with feedforward noise cancellation, the amplifier input-referred voltage noise density was reduced by about  $3\times$  over PVTs. The input-referred voltage noise density was less than 0.8 nV/sqrt(Hz) over a 30–120 MHz frequency range. The THD simulation was also performed, and the simulation results are summarized in Table 1. The signal generated by the transducer was in the range of 0.5–2 mV peak-to-peak, corresponding to an input signal power of  $-62$  dBm to  $-50$  dBm in a 50  $\Omega$

terminated system. As shown in Table 1, the complementary CMOS topology provided a THD improvement of larger than 9 dB across the input signal range.

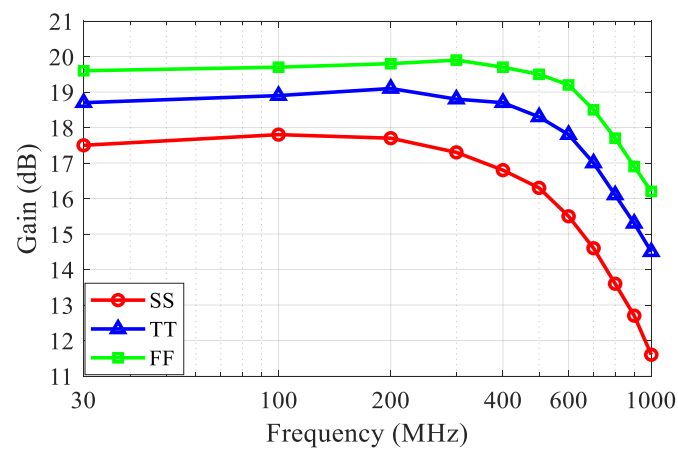


Figure 12. Simulated frequency response of the proposed LNA.

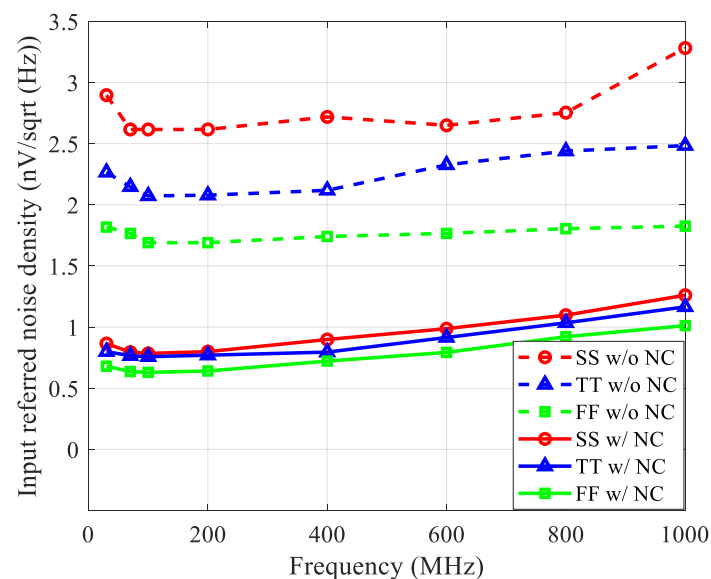


Figure 13. Simulated input-referred voltage noise density of the proposed LNA.

Table 1. Simulated THD of the LNA.

		$P_{IN}$ (dBm)	−62	−56	−50
THD (dBc) @ 80 MHz	NC only (NMOS)		−55.1	−49.1	−42.7
	NC only (PMOS)		−55.7	−49.6	−43.5
	NC with complementary		−65.3	−59.3	−53.7

## 5. Measurement Results and Analysis

A high-frequency ultrasound and photoacoustic imaging front-end, as shown in Figure 14, including the proposed LNA and a pseudo-differential VGA, has been developed and fabricated in a one-poly six-metal (1P6M) 180 nm bulk CMOS process with a core area of  $380 \mu\text{m} \times 350 \mu\text{m}$ . The gain of the VGA is programmable, ranging from 20 to 32 dB with a 6-dB gain step. The Figure 15 shows the die photo of the front-end. Figure 16 shows the measurements setup. The  $S_{11}$  and frequency response were measured with the Keysight N5247A network analyzer. The noise density and the THD were measured with the Keysight E4438C signal generator and the Keysight N9040B signal analyzer.

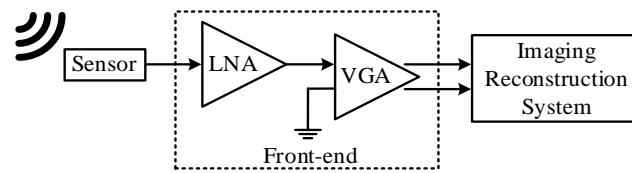


Figure 14. Block diagram of the HFUS and PA imaging front-end.

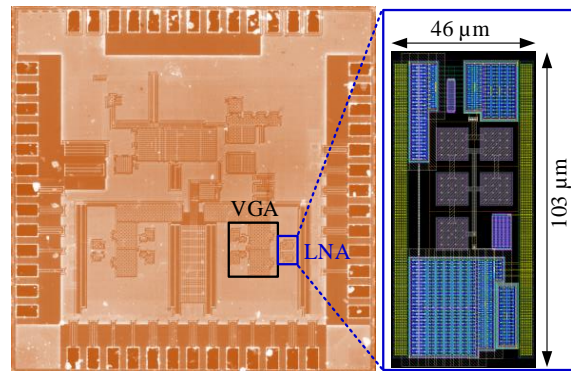


Figure 15. Die photo of the ultrasound front-end.

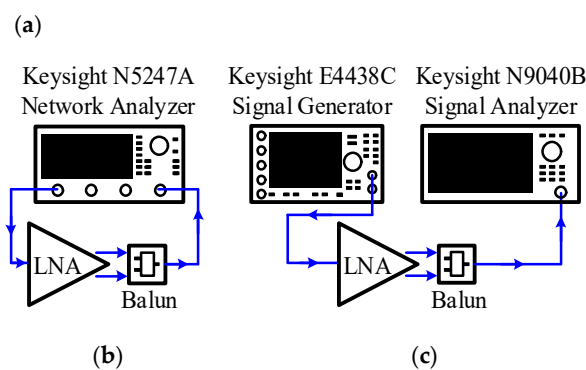
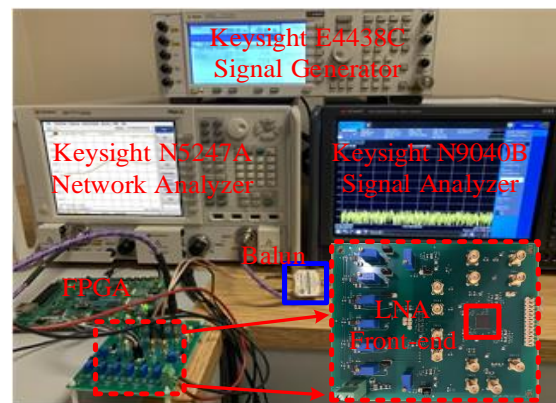


Figure 16. (a) Measurements setup; (b)  $S_{11}$  and frequency response measurement; and (c) noise density and THD measurement.

The Gain Method [25] has been applied to measure the NF. The NF in the Gain Method could be expressed as

$$NF = P_{NOUTD} + 174 \text{ dBm/Hz} - A_V, \tag{20}$$

where  $P_{NOUTD}$  is the measured output voltage noise density, 174 dBm/Hz is the noise density of 290°K ambient noise, and  $A_V$  is the measured front-end gain. Based on the measured NF, the corresponding input-referred voltage noise density,  $e_{NI}$ , in a 50  $\Omega$  terminated system was obtained as

$$e_{NI} = \sqrt{4kT \times R_{50} \times \left[ (10^{NF/10})^2 - 1 \right]}. \quad (21)$$

The measured  $S_{11}$  was better than  $-16$  dB over the frequency range of 30–120 MHz, as shown in Figure 17. Setting the VGA with a 20 dB gain, the measured frequency response of the front-end is shown in Figure 18. Due to the bandwidth limitation of the VGA, the measured  $f_{-3dB}$  bandwidth of the front-end was 89 MHz. The noise performance of the front-end over 30–120 MHz is shown in Figure 19. The measured input-referred noise density of the front-end was 1.36 nV/sqrt (Hz) at 80 MHz, which closely matched the simulation result of 1.26 nV/sqrt (Hz). Figure 20 shows the measured THD of the front end. With  $V_{IN,PP} = 1$  mV, the measured THD was better than  $-55$  dBc over 30–80 MHz and was  $-51$  dBc at 120 MHz.

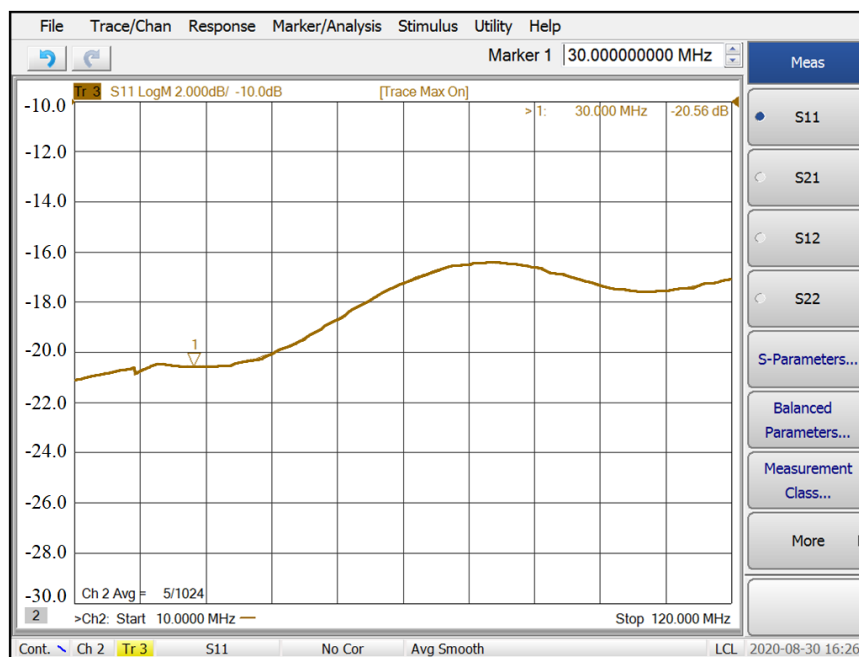


Figure 17. The measured  $S_{11}$  of the front-end.

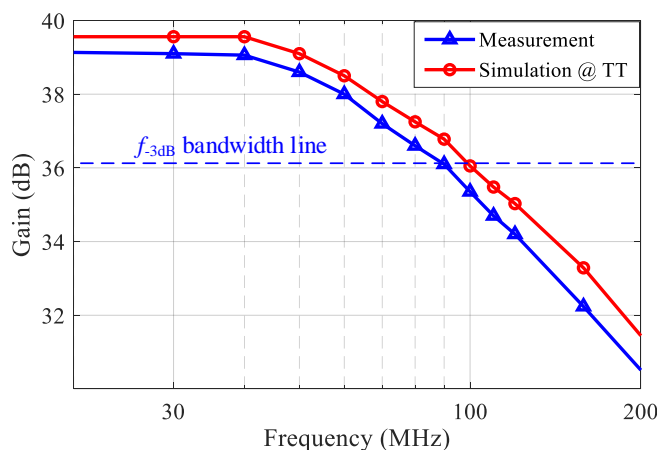


Figure 18. The measured frequency response of the front-end.

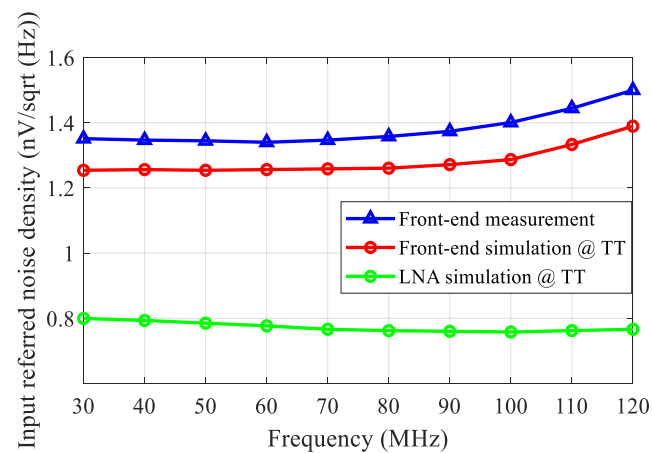


Figure 19. The measured input-referred noise density of the front-end.

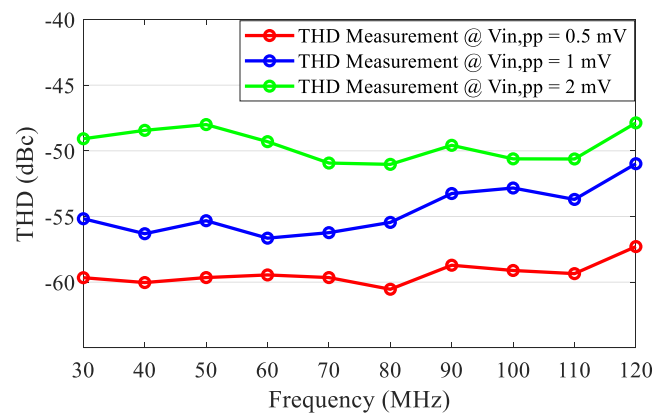


Figure 20. The measured THD of the front-end.

The noise efficiency factor [26], which considers the overall trade-off among noise, power consumption, and bandwidth, was obtained for the proposed front end. The noise efficiency factor was defined as

$$NEF = V_{NI,RMS} \cdot \sqrt{\frac{2I_{TOT}}{\pi \cdot V_T \cdot 4kT \cdot BW}} \quad (22)$$

where  $V_{NI,RMS}$  is the total input-referred voltage noise,  $I_{TOT}$  is the total current drained by the circuit,  $V_T$  is the thermal voltage, and  $BW$  is the front-end bandwidth. The input-referred noise of the front-end over 30–120 MHz was 14.2  $\mu$ V and the  $I_{TOT}$  was 20.56 mA. The NEF of the front-end was thus determined as 2.66.

Table 2 summarizes the performance of the front-end and compares it with recently published ultrasound amplifiers. The front-end achieved a low input-referred voltage noise density, a low THD, a high  $f_{-3dB}$  bandwidth, and competitive power consumption, demonstrating the best NEF.

**Table 2.** LNA front-end performance comparison.

Parameters	This Work *	[27] *	[28] **	[29] **	[30] *	[31] *	[32] *	[33] *
Process [nm]	180	180	28	180	130	350	350	180
Power supply [V]	1.8	1.8	1.0	1.8	3	3.3	±2.5	1.8
Bandwidth [MHz]	770 <sup>a</sup> /90 <sup>b</sup>	100	100	30	10	75	30	33
Gain [dB]	37	17.6	20	15.2	36	20	12	19.1
Input-referred noise density [nV/sqrt (Hz)]	1.36	4.19	1.74	3.5	7.41	2.68	6.3	1.01
Total input-referred noise [μV]	14.2	—	20.8	34.9	23.4	—	35.6	5.8
THD [dBc]	−55	—	—	—	—	—	—	−53.5
S <sub>11</sub> [dB]	−16	—	—	—	—	—	—	—
Power consumption [mW]	37	43	2	0.27	12.6	—	20	16.2
Noise efficiency factor	2.66	—	3.57	3.02	18.51	—	15.36	3.69
Core area [mm <sup>2</sup> ]	0.063	0.683	0.001	—	0.22	—	—	0.363

\* Measurement results; \*\* Simulation results. <sup>a</sup> LNA bandwidth; <sup>b</sup> Front-end bandwidth.

## 6. Conclusions

This paper presents a low-noise amplifier front-end for high-frequency ultrasound transducers. The LNA employs a resistive shunt-feedback configuration to simultaneously achieve a large  $f_{-3\text{dB}}$  bandwidth and a wideband impedance matching. To mitigate the noise in the resistive shunt-feedback amplifier, a feedforward noise-canceling technique was developed. A complementary CMOS topology was also developed to cancel the amplifier's second-order nonlinear distortion. An ultrasound receiver front-end, including the proposed LNA and a pseudo-differential VGA, was fabricated in a standard 180 nm CMOS process. Measured at 80 MHz, the front-end achieved an input-referred noise density of 1.36 nV/sqrt (Hz), a −16.4 dB input return loss, a 37 dB voltage gain, and a −55 dBc THD, while consuming 37 mW of power. The front-end demonstrated the best NEF with a large  $f_{-3\text{dB}}$  bandwidth, wideband impedance matching, low noise and harmonic distortion, and competitive power consumption, making it suitable for high-frequency ultrasound transducer applications.

**Author Contributions:** Conceptualization, Y.T., H.H., J.Z. and J.C.; methodology, Y.T., Y.F., H.H., C.F. and H.D.; validation, Y.T., Y.F., H.H., C.F. and H.D.; writing—original draft preparation, Y.T., Y.F., C.F., H.H. and H.D.; writing—review and editing, R.Z., J.Z. and J.C. All authors have read and agreed to the published version of the manuscript.

**Funding:** This research received no external funding.

**Institutional Review Board Statement:** Not applicable.

**Informed Consent Statement:** Not applicable.

**Data Availability Statement:** Data sharing is not applicable to this article as authors have used publicly available references, whose details are included in the “Measurement Results and Analysis” section of this article. Please contact the authors for further requests.

**Acknowledgments:** The authors thank the anonymous reviewers who helped to improve the quality of the paper.

**Conflicts of Interest:** The authors declare no conflict of interest.

## References

- Shung, K. High frequency ultrasonic imaging. *J. Med. Ultrasound* **2009**, *17*, 25–30. [[CrossRef](#)]
- Chandrana, C.; Talman, J.; Pan, T.; Roy, S.; Fleischman, A. Design and analysis of MEMS based PVDF ultrasonic transducers for vascular imaging. *Sensors* **2010**, *10*, 8740–8750. [[CrossRef](#)] [[PubMed](#)]
- Bitton, R.; Zemp, R.; Yen, J.; Wang, L.; Shung, K. A 3-D high-frequency array based 16 channel photoacoustic microscopy system for in vivo micro-vascular imaging. *IEEE Trans. Med. Imaging* **2009**, *28*, 1190–1197. [[CrossRef](#)] [[PubMed](#)]
- Daoudi, K.; Kersten, B.; Ende, C.; Hoogen, F.; Vonk, M.; Korte, C. Photoacoustic and high-frequency ultrasound imaging of systemic sclerosis patients. *Arthritis Res. Ther.* **2021**, *23*, 22. [[CrossRef](#)] [[PubMed](#)]



5. Kubelick, K.; Snider, E.; Ethier, C.; Emelianov, S. Development of a stem cell tracking platform for ophthalmic applications using ultrasound and photoacoustic imaging. *Theranostics* **2019**, *9*, 3812–3824. [[CrossRef](#)] [[PubMed](#)]
6. Strohm, E.; Moore, M.; Kolios, M. High resolution ultrasound and photoacoustic imaging of single cells. *Photoacoustics* **2016**, *4*, 36–42. [[CrossRef](#)] [[PubMed](#)]
7. Hsieh, B.; Chen, S.; Ling, T.; Guo, L.; Li, P. Integrated intravascular ultrasound and photoacoustic imaging scan head. *Opt. Lett.* **2010**, *35*, 2892–2894. [[CrossRef](#)] [[PubMed](#)]
8. O'Connor, P.; Geronimo, G. Prospects for charge sensitive amplifiers in scaled CMOS. In Proceedings of the IEEE Nuclear Science Symposium and Medical Imaging Conference, Seattle, WA, USA, 24–30 October 1999; pp. 88–93.
9. Li, X.; Zhang, Q.; Sun, Y. A low noise charge sensitive amplifier with adjustable leakage compensation in 0.18  $\mu\text{m}$  CMOS process. In Proceedings of the IEEE International Conference of Electron Devices and Solid-State Circuits, Hong Kong, China, 15–17 December 2010; pp. 1–4.
10. Chang, T.; Chen, J.; Rigge, L.; Lin, J. ESD-protected wideband CMOS LNAs using modified resistive feedback techniques with chip-on-board packaging. *IEEE Trans. Microw. Theory Tech.* **2008**, *56*, 1817–1826. [[CrossRef](#)]
11. Bruccoleri, F.; Klumperink, E.; Nauta, B. Wide-band CMOS low-noise amplifier exploiting thermal noise canceling. *IEEE J. Solid-State Circuits* **2004**, *39*, 275–282. [[CrossRef](#)]
12. Eriksrod, J.; Ytterdal, T. A 65nm CMOS front-end LNA for medical ultrasound imaging with feedback employing noise and distortion cancellation. In Proceedings of the European Conference on Circuit Theory and Design, Dresden, Germany, 8–12 September 2013; pp. 1–4.
13. Tang, Y.; Feng, Y.; Zuo, Z.; Fan, Q.; Fang, C.; Zou, J.; Chen, J. Wideband LNA with 1.9 dB noise figure in 0.18  $\mu\text{m}$  CMOS for high frequency ultrasound imaging applications. In Proceedings of the IEEE New Circuits and Systems Conference, Vancouver, BC, Canada, 26–29 June 2016; pp. 1–4.
14. Zhang, X.; Chen, Z.; Gao, Y.; Ma, F.; Hao, J.; Zhu, G.; Chi, B. An interference-robust reconfigurable receiver with automatic frequency-calibrated LNA in 65-nm CMOS. *IEEE Trans. Very Large Scale Integr. Syst.* **2017**, *25*, 3113–3124. [[CrossRef](#)]
15. Geha, C.; Nguyen, C.; Martinez, J. A wideband low-power-consumption 22–32.5-GHz 0.18- $\mu\text{m}$  BiCMOS active balun-LNA with IM2 cancellation using a transformer-coupled cascode-cascade topology. *IEEE Trans. Microw. Theory Tech.* **2017**, *65*, 536–547. [[CrossRef](#)]
16. Rahman, M.; Harjani, R. A sub-1V, 2.8 dB NF, 475  $\mu\text{W}$  coupled LNA for internet of things employing dual-path noise and nonlinearity cancellation. In Proceedings of the IEEE Radio Frequency Integrated Circuits Symposium, Honolulu, HI, USA, 4–6 June 2017; pp. 236–239.
17. Tang, Y.; Feng, Y.; Fan, Q.; Fang, C.; Zou, J.; Chen, J. A wideband complementary noise and distortion canceling LNA for high-frequency ultrasound imaging applications. In Proceedings of the IEEE Texas Symposium on Wireless and Microwave Circuits and Systems, Waco, TX, USA, 5–6 April 2018; pp. 1–4.
18. Zou, W.; Holland, S.; Kim, K.; Sachse, W. Wideband high-frequency line-focus PVDF transducer for materials characterization. *Ultrasonics* **2003**, *41*, 157–161. [[CrossRef](#)]
19. Foster, F.; Harasiewicz, K.; Sherar, M. A history of medical and biological imaging with polyvinylidene fluoride (PVDF) transducers *IEEE Trans. Ultrason. Ferroelectr. Freq. Control* **2000**, *47*, 1363–1371. [[CrossRef](#)]
20. Smolorz, S.; Grill, W. Focusing PVDF transducers for acoustic microscopy. *Res. Nondestruct. Eval.* **1996**, *7*, 195–201. [[CrossRef](#)]
21. Scholten, A.; Tromp, H.; Tiemeijer, L.; Langevelde, R.; Havens, R.; Vreede, P.; Roes, R.; Woerlee, P.; Montree, A.; Klaassen, D. Accurate thermal noise model for deep-submicron CMOS. In Proceedings of the International Electron Devices Meeting Technical Digest, Washington, DC, USA, 5–8 December 1999; pp. 155–158.
22. Nam, I.; Kim, B.; Lee, K. CMOS RF amplifier and mixer circuits utilizing complementary characteristics of parallel combined NMOS and PMOS devices. *IEEE J. Solid-State Circuits* **2005**, *53*, 1662–1671. [[CrossRef](#)]
23. Taris, T.; Begueret, J.; Deval, Y. A low voltage current reuse LNA in a 130 nm CMOS technology for UWB applications. In Proceedings of the European Microwave Integrated Circuit Conference, Munich, Germany, 8–10 October 2007; pp. 307–310.
24. Tang, Y.; Feng, Y.; Fan, Q.; Zhang, R.; Chen, J. A current reuse wideband LNA with complementary noise and distortion cancellation for ultrasound imaging applications. In Proceedings of the IEEE Asia Pacific Conference on Circuits and Systems, Chengdu, China, 26–30 October 2018; pp. 171–174.
25. Maxim Integrated. Noise Figure Measurement Methods and Formulas. Available online: <https://www.maximintegrated.com> (accessed on 5 November 2021).
26. Steyaert, M.; Sansen, W.; Chang, Z. A micropower low-noise monolithic instrumentation amplifier for medical purposes. *IEEE J. Solid-State Circuits* **1987**, *22*, 1163–1168. [[CrossRef](#)]
27. Yoon, J.; Lee, S.; Kim, J.; Song, N.; Koh, J.; Choi, J. Low-noise amplifier path for ultrasound system applications. In Proceedings of the IEEE Asia Pacific Conference on Circuits and Systems, Kuala Lumpur, Malaysia, 6–9 December 2010; pp. 244–247.
28. Luo, L.; Wu, Y.; Diao, J.; Ye, F.; Ren, J. Low power low noise amplifier with DC offset correction at 1 V supply voltage for ultrasound imaging systems. In Proceedings of the IEEE International Midwest Symposium on Circuits and Systems, Windsor, ON, Canada, 5–8 August 2018; pp. 137–140.
29. Diao, J.; Li, S.; Wu, Y.; Ye, F.; Xu, J.; Ren, J. Energy-efficient analog front-end design for ultrasound imaging applications. In Proceedings of the IEEE International Midwest Symposium on Circuits and Systems, Dallas, TX, USA, 4–7 August 2019; pp. 1171–1174.

30. Wang, Y.; Koen, M.; Ma, D. Low-noise CMOS TGC amplifier with adaptive gain control for ultrasound imaging receivers. *IEEE Trans. Circuits Systems. II Express Briefs* **2011**, *58*, 26–30. [[CrossRef](#)]
31. Kim, I.; Kim, H.; Griggio, F.; Tutwiler, R.; Jackson, T.; Trolier-McKinstry, S.; Choi, K. CMOS ultrasound transceiver chip for high resolution ultrasonic imaging systems. *IEEE Trans. Biomed. Circuits Syst.* **2009**, *3*, 293–303. [[CrossRef](#)] [[PubMed](#)]
32. Lay, L.; Carey, S.; Hatfield, J. Pre-amplifier arrays for intraoral ultrasound probe receiving electronics. In Proceedings of the IEEE Ultrasonics Symposium, Montreal, QC, Canada, 23–27 August 2005; pp. 1753–1756.
33. Jung, S.; Hong, S.; Kwon, O. Low-power low-noise amplifier using attenuation-adaptive noise control for ultrasound imaging systems. *IEEE Trans. Biomed. Circuits Systems* **2017**, *11*, 108–116. [[CrossRef](#)] [[PubMed](#)]